Heliyon 10 (2024) e24048

Contents lists available at ScienceDirect

Heliyon

journal homepage: www.cell.com/heliyon

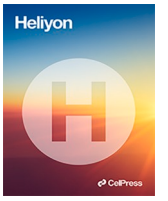

Research article

Calibration method of the k-ω SST turbulence model for wind turbine performance prediction near stall condition

Somaya Younoussi *, Abdeslem Ettaouil

Mechanical Engineering Department, Mohammadia School of Engineers, Mohammed V university, Rabat, Morocco

ARTICLE INFO

Keywords:
K–ω SST turbulence model
CFD
Wind turbine
Aerodynamic

ABSTRACT

The present study intends to enhance the accuracy of the k–ω SST turbulence model for numerical wind turbine simulation in stall condition. In order to achieve this purpose a calibration approach is proposed, and is applied to NREL S826 NTNU wind rotor. This method consists in adjusting the two turbulence model coefficients: α_1 and β^*, which are found to be 0.8 and 0.45 respectively. Then the calculated power and thrust coefficients are compared to the experimental results. The power coefficient results revealed that the simulation relative error at the range of tip speed ratio between 3 to 6 where light stall occurs, is reduced from 17.89 % to 4.58 % by application of calibration. The effects of calibration on flow behaviour are implemented thereafter, by analysing pressure, and skin friction coefficients distribution along the blade. The limiting streamlines on the blade suction side are examined for more flow behaviour understanding. The effects on turbulent kinetic energy around the blade are also highlighted. The main important conclusions that can be made is that calibration reduce the separation zone on the blade suction side, and limits the vortex shedding strength, leading to improve the rotor efficiency and hence to improve the model accuracy.

1. introduction

Wind power continues to be the major source of clean and renewable energy worldwide. As of 2022, 77.6 GW and 21 GW of onshore and offshore new wind turbines, respectively, were connected to grids, recording 906 GW of total installed wind capacity which helped the world avoid over 1.2 billion tons of CO_2 emissions [1]. However, despite these developments, 2022 also recorded a rise in CO_2 emissions, making the pathway towards the goals set by the Paris Agreement more challenging [1]. To stay on track towards these objectives, annual installations of wind turbines need to increase fourfold. This requires concerted effort across different wind energy areas, particularly in technological advancements. Over the last few decades, there have been significant advancements in wind turbine technology and it is further improving to make electricity generation more reliable, efficient and cost-effective. These developments include enhancing rotor blade aerodynamics-the power prediction and the structural design-, utilizing new materials, integrating new technologies for control monitoring and maintenance, and implementing smart rotor blades.

As aerodynamic is one of the most important aspects of wind turbine technology development, different theories have been implemented, tested and improved including the Blade Element Momentum (BEM) theory, the vortex wake method, wind tunnel experiments, and computational fluid dynamics (CFD). BEM and CFD theories are widely used for wind turbines performance predicting. The BEM method is particularly preferred by major wind turbine manufacturers due to its simplicity and computational cost

* Corresponding author.
E-mail address: somayayounoussi@research.emi.ac.ma (S. Younoussi).

https://doi.org/10.1016/j.heliyon.2024.e24048
Received 13 September 2023; Received in revised form 23 November 2023; Accepted 2 January 2024
Available online 4 January 2024

efficiency. However, BEM theory often fails to accurately predict the aerodynamics of Horizontal-Axis Wind Turbines (HAWT). With the huge advancement in processors power and numerical modelling tools performances, the CFD method has been recognised as a valuable asset for engineers and scientists of a large range of applications [2]. Nevertheless, CFD still faces some challenges, among which turbulence modelling which is one of the most intriguing problems in engineering and physics.

Turbulence modelling in CFD simulations involves selecting a numerical method which takes nonlinear convective terms in the Navier-Stokes equations into account. There are many numerical approaches such as Reynolds-Averaged Navier-Stokes (RANS), Large Eddy Simulation (LES) and Direct-Numerical Simulation (DNS) models. The DNS method [3] provides the most accurate results because it solves the Navier-Stockes equations without any additional modelling, it captures all the scales in a given flow, from small to large eddy sizes. Meanwhile, the required computer capacity is extremely large, and it increases sharply with Reynolds number. Therefore, its application is restricted to low-Reynolds number and small size computational domain problems. The main objective of LES method [4] is to reduce the computational cost of numerical simulations by neglecting the smallest scale eddies, and computing only large-scale ones in a turbulent flow. However, its computational demand is still too high for most practical uses. Due to its low computing requirements and relative accuracy in many aerodynamics applications, RANS model presented the backbone turbulence model in the industrial CFD applications for long time and is still considered as the most practical alternative for turbulence modelling [5].

Flow around a horizontal axis wind turbine blade is known to be highly complex because of the simultaneous presence of different phenomena. Due to these phenomena, the wind turbine RANS numerical simulations face a problem of poor accuracy especially when the phenomenon is resulting from turbulence. One of the most challenging problems for RANS is stall phenomenon prediction, which is investigated by the modelling of turbulence in the boundary-layer of the blade. Stall is characterised by a loss of lift caused by an excessive angle of attack, that leads to boundary layer separation on the blade's suction side. Rahimi et al. [6] investigated a steady-state RANS-based simulations to analyse the aerodynamic behaviour of stall regulated NREL phase VI rotor using OpenFOAM. In this study, the k–ω SST model reported properly the power, the thrust, the normal and the tangential forces coefficients. A deviation of numerical results was observed at 10 m/s, which was supposed to be due to stall phenomenon that generates a highly unstable flow behaviour at this wind speed. Zhang et al. [7] elaborated a comparison between DDES and RANS methods in order to predict the aerodynamic loads of the MEXICO rotor under stall condition at TSR = 4.17 using Open FOAM CFD open source. At this case, it was found that RANS method combined with k–ω turbulence model in comparison with DDES method failed to predict the normal force on the blade surface because of highly separated flow captured in this condition. More recently, Purohit et al. [8] evaluated the aerodynamic performance of the 3D full (New) MEXICO rotor using uRANS and LES. The results of the pressure coefficient distribution at V = 24 m/s ($\lambda = 4.17$) where stall occurs revealed that the separation onset point was better captured by LES method in comparison with uRANS.

In order to overcome the discrepancy between numerical and experimental results in stall condition, one of the remedies is to calibrate the parameters of the turbulence model. For instance, many research studies were adopted this solution and applied it to k–ω SST model which is very popular for wind turbines aerodynamics prediction. Rocha et al. [9] proposed a calibration of the k–ω SST turbulence model by testing several values for β* coefficient, for a three-bladed wind turbine NACA 0012 constructed and operated at the Federal University of Ceará. The results revealed that calibration of the model wasn't affected by the turbulence intensity and the turbulence characteristic length scale. Whereas, the variation of β* had significant impacts on the blade's surface viscous friction, leading as a result to an improvement of the wind turbine model efficiency. In this analysis the k–ω SST turbulence model was adjusted with adopting 0.45 for β* coefficient. The same method was thereafter re-tested by Rocha et al. [10] for two different kinds of small-scale wind turbines geometries. The first turbine was designed with symmetrical NACA 0012 airfoil, and the second one was designed with cambered NACA4412 airfoil. The numerical simulation was investigated using CFD code Open Foam. In this study, the model calibration was evaluated at all operational range of tip speed ratio ($0 < \lambda < 8$). For both turbines, it was observed that at low tip speed all the β* tested value worked well. Whilst, by increasing rotation, the effectiveness of the calibrated model starts to perceived because of the dominance of the moment due to drag forces. Among all the numerically tested β* values, 0.27 showed the lowest error value. Another calibration method was used by Matyushenko and Garbaruk [11] in order to predict the airfoil characteristic near stall. As the a_1 constant plays a decisive role in flow behaviour control, the author selected the coefficient a_1 to be calibrated. This method was tested on four aerodynamic airfoils with different shapes and thicknesses. The decrease of a_1, increased the recirculation zone size owing to enhance the accuracy of the results over a wide range of angles of attack. However, the authors showed that the adjustment of the turbulence model coefficient affects the original model calibration, an inaccuracy was obtained when analysing skin friction coefficient for simple wall-bounded turbulent flows. Another calibration method was proposed by Zhong et al. [12] in order to improve the simulation accuracy of wind turbine stall. A steady-state RANS model was investigated using k–ω SST turbulence model as closure. The calibration was firstly applied on the S809 airfoil and then was tested on the NREL Phase VI 3d rotor. In this approach, the β^* coefficient was adopted to be adjusted. The results of the S809 airfoil simulations showed that the lift coefficient prediction error was reduced to 4.5 % from 30 % in light stall conditions when the β* was calibrated to 0.11. The same adjustment was tested on the 3d rotor, it was recognised that at low to medium wind speeds under light stall condition, a good accuracy of rotor aerodynamic prediction was observed.

In the light of the above literature review, calibration method remained an important solution to accurately predict stall using wind turbines RANS simulations. The present work intends to improve k–ω SST turbulence model in stall condition. For this purpose, a new calibration method is proposed which aims to create a balance between the two important k–ω SST model coefficients a_1 and β*. Different adjustments cases are tested on NREL S826 NTNU wind turbine to achieve the optimal values of the precited coefficients. The results in terms of power and thrust coefficients are compared to experimental data. Then, an analysis of calibration effects on flow behaviour, and turbulent kinetic energy around the blade is performed. The proposed method increases the accuracy of k–ω SST

turbulence model in predicting wind turbine aerodynamic in stall condition which is still debatable.

2. computational method

2.1. Turbulence model

Performed by Menter in 1994 [13], k–ω SST turbulence model is a hybrid model combining two turbulence models: the k–ω of Wilcox and the k-ε of Launder and Spalding [14]. The k–ω model is used near the wall because it provides good prediction of the flow behaviour near the boundary layer, and k-ε is used away from the wall due to its good accuracy in these regions. Likewise, the SST model improves the accuracy of adverse pressure gradients prediction and limits the high sensitivity of original k–ω to free stream flow. The k–ω SST is governed by two transport equation, one for the turbulence kinetic energy k and the other for the turbulence specific dissipation rate ω:

$$\frac{\partial}{\partial t}(\rho k)+\frac{\partial}{\partial x_i}(U_i\rho k)=\frac{\partial}{\partial x_j}\left((\mu+\sigma_k\mu_t)\frac{\partial}{\partial x_j}k\right)+\widetilde{P_k}-\beta^*\rho\omega k, \tag{1}$$

$$\frac{\partial}{\partial t}(\rho\omega)+\frac{\partial}{\partial x_i}(U_i\rho\omega)=\frac{\partial}{\partial x_j}\left((\mu+\sigma_\omega\mu_t)\frac{\partial}{\partial x_j}\omega\right)+\frac{\rho\gamma}{\mu_t}S^2-\beta\rho\omega^2+2\rho(1-F_1)\frac{1}{\omega}\frac{1}{\sigma_{\omega,2}}\frac{\partial}{\partial x_j}k\frac{\partial}{\partial x_j}\omega, \tag{2}$$

In order to avoid the production of excessive turbulence in stagnation points, a production limiter is used in this turbulence model. The production term is hence expressed as follow:

$$P_k=\mu_t\frac{\partial u_i}{\partial x_j}\left(\frac{\partial u_i}{\partial x_j}+\frac{\partial u_j}{\partial x_i}\right)\quad\rightarrow\quad\widetilde{P_k}=\min(P_k,10.\beta^*\rho k\omega), \tag{3}$$

One of the most important additions that Menter has bring through the SST model is that the inclusion of a transport equation for turbulent shear stress by adopting Johnson-King (JK) model [15]. The JK model is based on Bradshaw assumption which assumes that the turbulent shear stress in a boundary layer τ is proportional to the turbulent kinetic energy k like illustrated in Equation (5). The Menter's SST model uses this hypothesis to define a new expression of eddy-viscosity illustrated in Equation (6). This modification leads to enhance the accuracy of strong adverse pressure gradient flows prediction.

$$\tau=\rho a_1 k \tag{4}$$

Where a_1 is the structure coefficient and it is a constant.

The new eddy-viscosity expression is:

$$\mu_t=\frac{\rho a_1 k}{\max(a_1\omega,SF_2)} \tag{5}$$

Where $S=\frac{\partial U_i}{\partial x_j}$ is the invariant measure of the strain rate, and F_2 is equal to zero in the flow boundary-layers and 1 in the flow free layers and it is given by:

$$F_2=\tanh\left(\left\{\left[\max\left(\frac{2\sqrt{k}}{0.09\omega y};\frac{500\nu}{y^2\omega}\right)\right]\right\}\right) \tag{6}$$

The F_1 is expressed as:

$$F_1=\tanh\left(\left\{\min\left[\max\left(\frac{\sqrt{k}}{0.09\omega y};\frac{500\nu}{y^2\omega}\right);\frac{4\rho\sigma_{\omega 2}k}{CD_{k\omega}y^2}\right]\right\}\right) \tag{7}$$

$$\text{Where } CD_{k\omega}=\max\left(2\rho\frac{1}{\omega}\frac{1}{\sigma_{\omega 2}}\frac{\partial k}{\partial x_i}\frac{\partial\omega}{\partial x_i};10^{-10}\right) \tag{8}$$

The rest of constant are calculated using the equation bellow:

$$\varphi=\varphi_1F_1+\varphi_2(1-F_1)$$

The parameters (φ_1) from the original k–ω model is:

$\gamma_1=\left(\frac{\beta_1}{\beta^*}\right)-\left(\frac{\sigma_{\omega 1}\kappa^2}{\sqrt{\beta^*}}\right)=0.5532$, $\boldsymbol{\sigma_{k1}}=0.85$, $\boldsymbol{\sigma_{\omega 1}}=0.5$, $\boldsymbol{\beta_1}=0.075$,

The parameters (φ_2) from the transformed k-ε model are:

$\gamma_2=\left(\frac{\beta_2}{\beta^*}\right)-\left(\frac{\sigma_{\omega 2}\kappa^2}{\sqrt{\beta^*}}\right)=0.44$, $\sigma_{k2}=1.0$, $\boldsymbol{\sigma_{\omega 2}}=1.168$, $\beta_2=0.0828$;

The constants values are given as follows:

$a_1=0.31$, $\beta^*=0.09$, $\kappa=0.41$.

2.2. Numerical method

In the present work, Ansys Fluent CFD solver is used to perform the NREL S826 NTNU wind turbine performance calculations. The three-bladed 0.894 m diameter NTNU BT1 turbine geometry is based on a twisted and tapered NREL S826 airfoil [16], with a pitch angle of 0°. The distribution of the chord and the twist angle along the blade are presented in Fig. 1, and the blade shape is shown in Fig. 2. Table 1 summarized the main characteristics of the used blade.

The numerical results have been obtained from the resolution of the Reynolds-Averaged Navier–Stokes (RANS) equations combined with the k–ω SST turbulence model [13]. The single reference frame (SRF), is used to simulate rotor rotation. The governing equations of the present model can be written in the framework of SRF as follow:

$$\nabla \overrightarrow{V_r} = 0, \tag{9}$$

$$\nabla\left(\overrightarrow{V_r} \otimes \overrightarrow{V_r}\right) + 2\left(\overrightarrow{\Omega} \otimes \overrightarrow{V_r}\right) + \left[\overrightarrow{\Omega} \otimes \left(\overrightarrow{\Omega} \otimes \overrightarrow{r}\right)\right] = \rho \overrightarrow{f} - \nabla p + (\mu + \mu_t)\nabla.\nabla\left(\overrightarrow{V_r}\right), \tag{10}$$

where $\overrightarrow{V_r} = \overrightarrow{V_a} + \overrightarrow{\Omega} \otimes \overrightarrow{r}$ is the velocity in the rotating frame. $2(\overrightarrow{\Omega} \otimes \overrightarrow{V_r}) + [\overrightarrow{\Omega} \otimes (\overrightarrow{\Omega} \otimes \overrightarrow{r})]$ presents the Coriolis and centrifugal accelerations, $\overrightarrow{f}$ is the gravity vector, p is the pressure; μ and μt are respectively the kinematic and the turbulent kinematic viscosity of the fluid.

For the purpose of reducing computational time, only one blade is modelled since the flow around the rotor is symmetric. The blade geometry was imported into a computational fluid domain, which is one-third of a cylinder with periodic faces to consider the effects of the other two blades, as shown in Fig. 4. The diameter of the fluid domain is 3d and its length is 6d where d is the rotor diameter. The upstream inlet boundary was defined at 2d in front of the blade. Whereas, the downstream outlet boundary was specified at offset 4d behind the blade.

The Ansys meshing is used to create a structured prismatic mesh around the blade surface and an unstructured tetrahedral mesh in the rest of the fluid domain. As the resulting fluid flow near the rotor is far more complex, a finer mesh is generated around the blade using a sphere of 0.6 m radius and a mesh size 0.03 m as a body of influence. The turbulence model used in the present work necessitated a value of wall y + around 1 to capture the boundary layer behaviour [17]. Hence, 20 inflation layers with first layer thickness of 0.00825 mm and growth rate of 1.25 were created around the blade surface. The generated mesh is illustrated in Fig. 3. In advance of the study, it was essential to conduct a mesh sensitive analysis by testing seven different mesh sizes on the blade surface: 4.4 mm, 3.4 mm, 2 mm, 1.5 mm, 1.2 mm, 1.15 mm, and 1.01 mm by monitoring mechanical torque. For its low computational time cost, the Spalart-Allmaras [18] turbulence model is used in the mesh sensitivity study.

In this simulation, the inlet velocity was specified as 10 m/s. In the outlet boundary layer, zero-gauge static pressure was applied. The blade surface was defined as a wall with no-slip boundary condition, and it was considered in rotation according to the absolute frame with zero angular velocity.

The steady-state, pressure-based method was used in combination with absolute velocity formulation to solve the incompressible RANS model. A semi-implicit method SIMPLE [19] was used to model the velocity and pressure in momentum and continuity equations in a segregated manner.

The second-order upwind was used for solving both viscous terms and convective terms. The least squares cell-based method was applied for spatial discretization gradient scheme. A second order discretization scheme was employed in the pressure values interpolation. This interpolation scheme minimizes the numerical diffusion and also boosts accuracy.

Standard initialization method is used in these simulations, where the inlet boundary layer was used for calculating the initial values. Once convergence was obtained, the power and thrust coefficients output results were validated against experimental data.

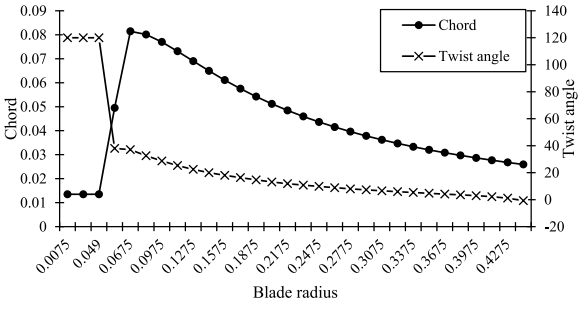

Fig. 1. Chord and twist angle distribution along the blade.

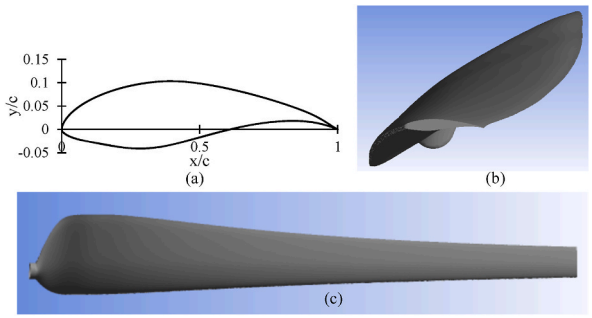

Fig. 2. The blade shape: (a) Shape of NREL S628 airfoil; (b) Twisted sections; (c) Blade suction side.

Table 1
Characteristics of the wind turbine blade.

Parameters	Values
Airfoil profile	NREL S628
Designed wind speed	10 m/s
Designed tip speed ratio	6
Pitch angle	0°
Rotor diameter	0.894 m
Number of blades	3
Turbulence intensity	0.3 %

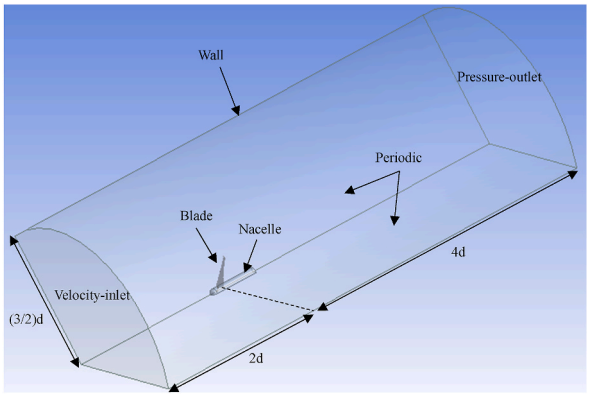

Fig. 3. Computational fluid domain and boundary condition.

3. Results and discussion

3.1. mesh study

In grid study, seven meshes are tested by monitoring mechanical torque. The blade meshing is refined in order to get convergence, starting with 4.4 mm element size to 1.01 mm as presented in Table 2. The increase in fineness of blade mesh enhances the mesh quality but at the same time increases the number of elements which automatically increases the computational time. The variation of torque with number of elements is illustrated in Fig. 5. It is clearly observed that at a size of 1.2 mm the results start to converge. Consequently, the blade element size adopted for the present CFD model is 1.2 mm.

3.2. model validation

The CFD simulation of NREL S826 NTNU turbine is carried out at different tip speed ratios varying from 1 to 12. Fig. 6presents the calculated results in comparison with measured ones. At low tip speed ratio values, the numerical results show good agreement with experimental data. In the range of $3 < \lambda < 6$, the present simulation underpredicts the power coefficient. Whereas, in the range of $6 < \lambda < 10.5$, the power coefficient is accurately predicted and it reaches its maximal value at $\lambda = 6$. At high TSR values corresponding to $\lambda > 10.5$, the results are again underestimated. The thrust coefficient is accurately predicted at low TSR values. Starting with 4 the obtained

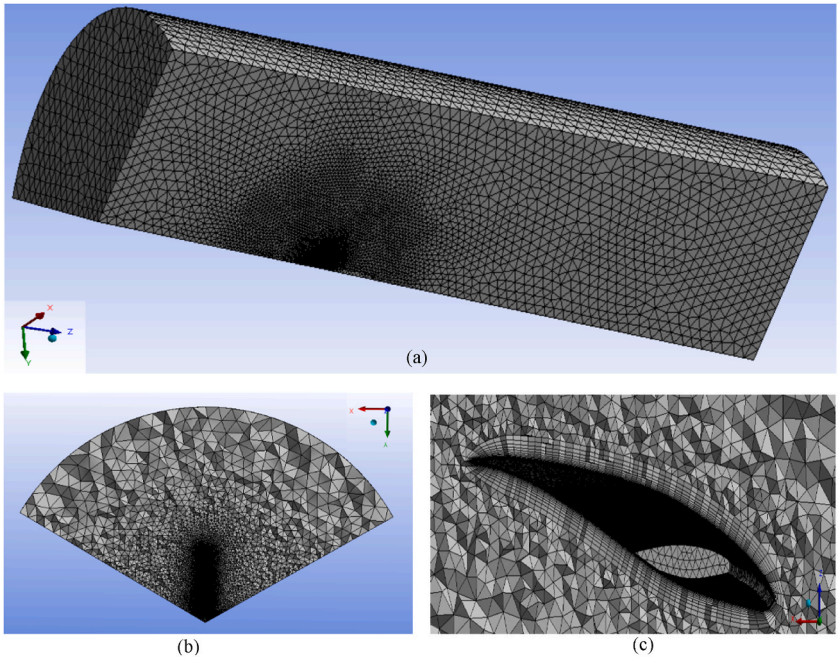

Fig. 4. View of the adopted mesh in (a) the fluid domain, (b) sectional plane, and (c) close to the blade surface showing inflation layers.

Table 2
Mesh convergence study.

Blade Element size	Number of elements	Orthogonal quality	Skewness	Torque (N.m-1)	Thrust (N)
4.4 mm	859198	0.746	0.239	−0.223	9.527
3.4 mm	1046034	0.743	0.242	−0.293	10.074
2 mm	1,857,086	0.757	0.232	−0.357	10.423
1.5 mm	2,602,079	0.765	0.227	−0.369	10.463
1.2 mm	**3,269,683**	**0.769**	**0.225**	**−0.384**	**10.533**
1.15 mm	3,710,891	0.773	0.222	−0.389	10.597
1.01 mm	4,054,859	0.776	0.219	−0.389	10.555

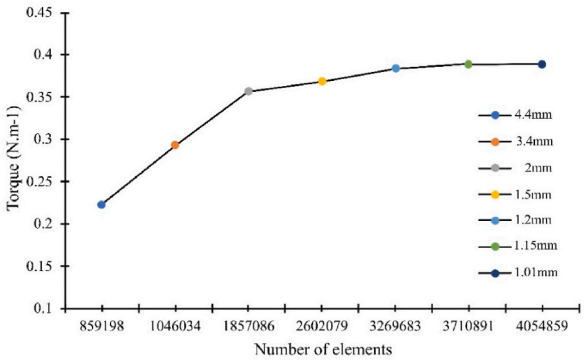

Fig. 5. Variation of the torque with the number of elements.

curve deviates from the measured one. The highest errors are recorded at 4, 5 and for the range of $\lambda > 9$.

In order to analyse the flow behaviour around the blade, the limiting streamlines on the blade suction side at different tip speed ratio are plotted in Fig. 7. At $\lambda = 3$, all lines are curved indicating that the flow is totally separated, hence the blade is under deep stall condition. At $\lambda = 4$, and 5.1 the separation zone is reduced, this means that the blade is lightly stalled. When tip speed ratio attains its maximum, the flow remains completely attached. The same observation is done when $\lambda = 10.2$. In comparison with the power coefficient results, it can be seen that the results are well predicted when the flow is under deep stall condition and when it is totally

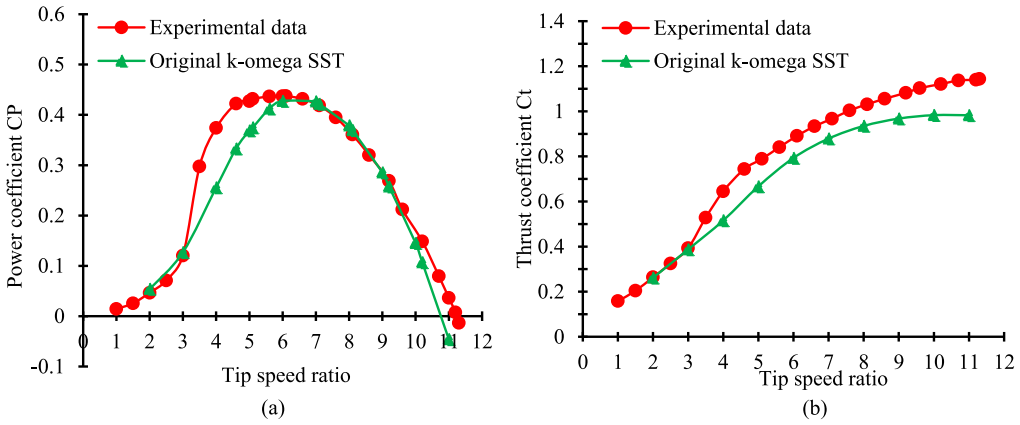

Fig. 6. Comparison of the predicted power (a) and thrust (b) coefficients with experimental data at different tip speed ratio.

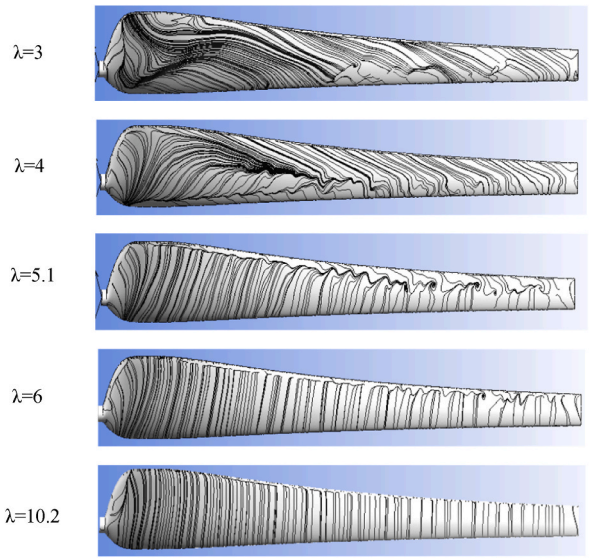

Fig. 7. Limiting streamlines on the blade suction side.

attached to the blade. Whereas, an important model's failure is recorded when light stall occurs. In order to reduce the discrepancy between calculated and measured results when light stall occurs, a calibration method of the k–ω SST turbulence model will be proposed and discussed later.

3.3. model calibration

The present study aims to improve the k–ω SST turbulence model accuracy in light stall conditions, which occurs in the range of $3 < \lambda < 6$. One of the solutions, is the calibration of the turbulence model by adjusting the most impactable coefficients. Stall phenomenon is related to separation which is monitored by the modelling of turbulence in the boundary layers. Since k–ω SST is an eddy-viscosity turbulence model, which is based on Boussinesq eddy-viscosity approximation, the control of separation phenomenon depends on eddy-viscosity estimation. By the application of Bradshaw's assumption, Menter [13] introduced Equation (5) to correct the eddy-viscosity expression. But even though in separated flow, the eddy-viscosity remained underestimated leading to advancing separation and lagging reattachment [20] which extend the separation zone and underestimates the numerical results. According to Bai et al. work [20], the reason of the advanced separation is related to the fact that Bradshaw's assumption enforces a turbulent energy equilibrium condition in all areas, which is harsh in regions affected by large pressure gradient. Whereas, the reattachment lagging is found to be due to the main strain rate [20] which influences turbulent kinetic energy generation. Based on Bai et al. findings, a calibration method is proposed in the present work in order to enhance the efficiency of k–ω SST turbulence model in stall condition by adjusting the coefficients: a_1 and β*.

The coefficient a_1 is the factor of proportionality between turbulent shear-tress and turbulent kinetic energy in a boundary layer as shown by Equation (4). Therefore, the simulated flow behaviour in such boundary layer is controlled by a_1. Whereas, the coefficient β* is included in the kinetic energy production and dissipation terms as expressed by Equation (3) and (1) respectively. Therefore, the coefficient β* can directly affected the production and the dissipation of the turbulent kinetic energy which are due to the viscous forces that governed the model behaviour in such boundary layers.

According to Menter et al. [21], the coefficient a_1 can be varied in k-ω SST steady-state simulation. Meanwhile, Menter et al. assumed that only the increase of a_1 is allowed because its decrease affects negatively the original flat-plate calibration of the model. They found that an a_1 of 1 can reduce flow separation. In the presence of large pressure gradients (stall), the ratio of production to dissipation of turbulent kinetic energy is significantly larger than one which means that: $\widetilde{P_k} \gg D_k$ [22], hence the a_1 and β* must satisfy: $\beta^* \ll {a_1}^2$ in this condition.

In search of optimal a_1 and β* values, the a_1 coefficient is firstly increased by 0.1 starting from 0.4 while keeping the original value of β* constant and the power coefficient of the blade is calculated at tip speed ratio of 4. The numerical results in term of power coefficient are depicted in Fig. 8 (a). It is observed that the calculated power coefficient increases rapidly with a_1, and starts to converge at $a_1 = 0.6$. A jump from 0.256 to 0.292 in power coefficient is achieved at a_1 of 0.6, reducing hence the relative simulation error as defined in Ref. [12] by nearly 10 %.

Then, a second adjustment is attributed to β^* model's coefficient for the four a_1 values where the power coefficient remained stable: 0.6, 0.7, 0.8, 0.9. Fig. 8 (b) shows the variation of power coefficient with β^* coefficient. It is observed that the power coefficient corresponded to all a_1 values increases rapidly until reaching a peak, and then falls down. The maximum peak of 0.335 is recorded at a_1 of 0.9 and β* of 0.55. Fig. 9 illustrates a comparison between calibrated models and the original k-ω turbulence model at tip speed ratio between 3 and 6. Both the calibrated models 1 and 2 improve the results of the numerical simulations at this range of tip speed ratio and their slopes seem similar. They slightly diverge from each other when the flow starts to be totally attached at tip speed ratio of 6.1 and 8.1. The attached flow is characterised by the dominance of frictional effects which leads to an elimination of pressure gradient effects and to a creation of turbulent kinetic energy equilibrium in boundary layers [23]. The turbulent eddy-viscosity in this condition is independent of coefficient a_1 [24]. The effects of β*, which is supposed to impact the flow behaviour in the boundary layers, is suppressed by the simultaneous calibration of a_1. Table 3 proves this finding by testing calibrated models at tip speed ratio of 8.1, the results show that when only the β* is increased and a_1 is of original value of 0.31(Model 3), the predicted power coefficient decreases significantly. The slight deviation between the calibrated models results and the original one is due to the effects of these coefficients on the separated flow at the blade trailing edge as it is shown in Fig. 7. Finally, according to Fig. 9, the calibrated model whose results agree with experimental data with the lowest errors in light stall and no stall conditions is the model 1. As a result, the optimal values of $a1$ and β* in this case study are found to be 0.8 and 0.45 respectively. This calibration method helps to reduce the relative error at tip speed ratio of 4 by approximately 20 %. This finding demonstrates that the blade performance prediction can be enhanced by an adjustment of the turbulence model coefficients $a1$ and β*.

3.4. power and thrust

The calculated power coefficient using the calibrated k–ω SST turbulence model is plotted against tip speed ratio in Fig. 10 (a). At high tip speed ratio values, the calibrated model seems close to original one, and both the two models show good agreement with experimental data. Whereas, at very high tip speed ratio exceeding 10, the both models failed to predict the results. At low tip speed varying from 1 to 3 where the flow is under deep stall phenomenon, the results of original model looks better than that of calibrated one. In the range of tip speed ratios between 3 and 6, where light stall occurs, the calibrated model predicts more accurate results in comparison to original model, and helps hence to reduce the relative simulation error in this range from 17.89 % to 4.58 % as shown in Table 4. It can be concluded that the calibration enhances the blade efficiency in stall or near stall conditions, but has no effects when the flow is fully attached.

The results of thrust coefficients versus tip speed ratio are shown in Fig. 10 (b). Thanks to the new turbulence model calibration, the

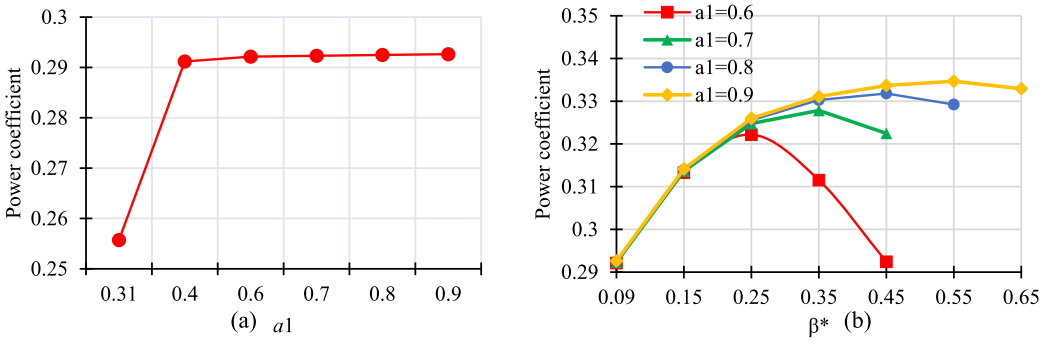

Fig. 8. Power coefficient variation with: (a) a1 and (b) β*.

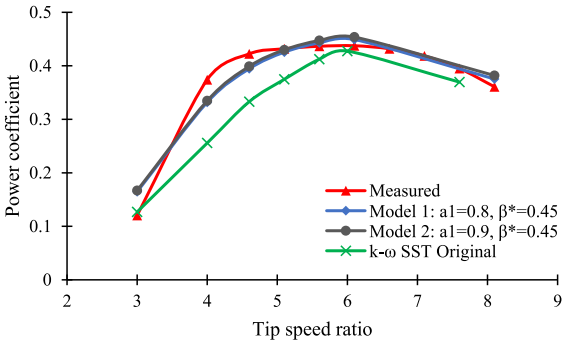

Fig. 9. Comparison between calibrated models and original model in term of power coefficient.

Table 3
Power coefficient at tip speed ratio of 8.1 calculated by different turbulence models.

Tip speed ratio	Measured	k-ω SST Original	Model 1: $a1 = 0.8$, $\beta^* = 0.45$	Model 2: $a1 = 0.9$, $\beta^* = 0.45$	Model 3: $a1 = 0.31$, $\beta^* = 0.45$
8.1	0.3608	0.3695	0.3752	0.3817	0.3188

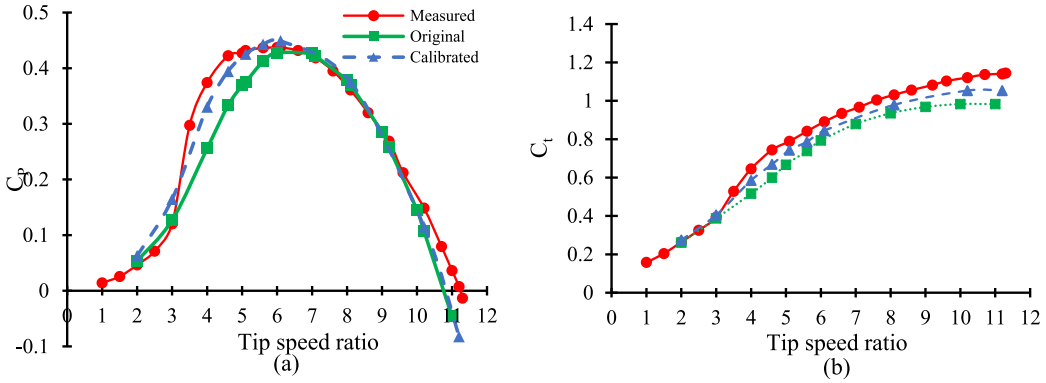

Fig. 10. Comparison of the numerical power (a) and thrust (b) coefficients results resulted from original and calibrated models with measured.

Table 4
The relative simulation error of the rotor power coefficient for original and calibrated turbulence model.

Tip speed ratio	3	4	4.6	5.1	5.6	6	Total error
$a_1 = 0.31$, $\beta^* = 0.09$	5.46 %	31.64 %	21.16 %	13.22 %	5.54 %	2.18 %	17.89 %
$a_1 = 0.8$, $\beta^* = 0.45$	36.79 %	11.70 %	6.61 %	1.47 %	1.44 %	2.66 %	4.58 %

results become more closer to measured ones at different tip speed ratio. However, at very high tip speed ratio values the both models are unable to accurately predict thrust coefficient.

3.5. effects of calibration on flow behaviour

3.5.1. pressure coefficient

Fig. 11 shows the effects of a_1 variation on pressure coefficient distribution at different radial positions. In the root region where r/R = 0.22, and 0.32, all tested models present similar distribution of pressure around the blade due to the smallness of area affected by separation. Beyond r/R = 0.48, a difference between original and calibrated models' results appears particularly near leading edge. The discrepancy between the graphs increases with radial position. The area enclosed by the Cp graph increases near leading edge while near the trailing edge it shrinks indicating that the lift force increases near the leading edge and is limited near the trailing edge because the lift force is created by the pressure difference between the upper and lower surfaces. The most important variation of Cp is observed near blade tip since the pressure force acting close the blade tip has more significant contribution in the power production.

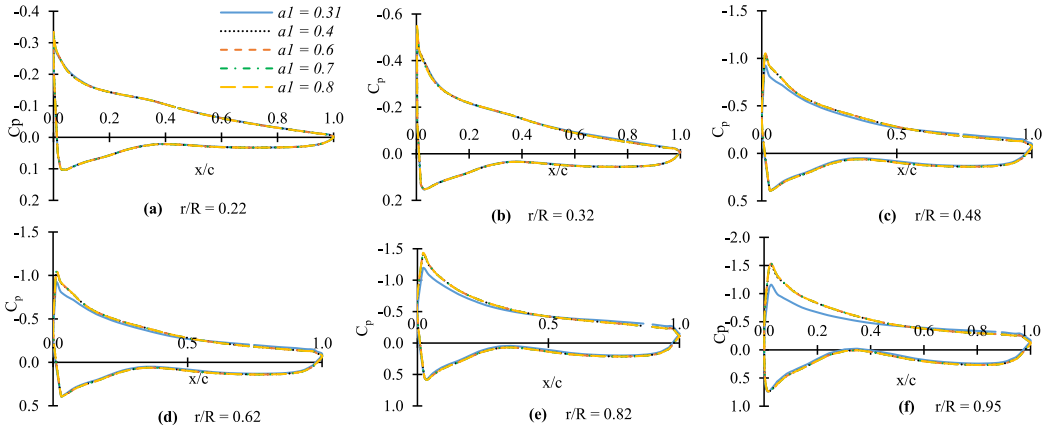

Fig. 11. Pressure coefficient distributions for different values of a_1 at $\beta^* = 0.09$.

The same observations are done when a_1 is fixed at optimal value of 0.8, while the β* is varied as illustrated in Fig. 12. It is observed that near the tip region the area enclosed by Cp graph further increases when β* increases denoting that the blade efficiency is more performed by the β* adjustment.

3.5.2. 2- skin friction

Figs. 13 and 14 depict the effects of a_1 on skin friction along the blade suction side. Fig. 13 shows a subtle difference between original and calibrated models results close to hub at r/R = 0.22, where the majority of the flow is attached. Because of the presence of separation, the increase of a_1 reduces the shear stress at r/R = 0.48, 0.62, 0.82 and 0.95 in the boundary. The limiting streamlines are displayed in Fig. 10. It is observed that the separation is pushed downstream due to a_1 increase, reducing hence the separation zone on the blade. The shear lines inclination decreases with calibration indicating a decrease in the centrifugal force's effects. The effects of β* on skin friction distribution along the blade suction are illustrated in Figs. 15 and 16. By analysing Fig. 15, it is observed that along the blade the peak near the leading-edge advances upstream with the increase of β*, causing thus an early flow reattachment. This finding indicates that calibration shortens the separation bubble until its elimination due to the increase of the eddy viscosity [25]. The limiting streamlines plotted in Fig. 14 show clearly this finding. As a results, the zone of attached flow rises and enhances the rotor efficiency. In contrast with the effects of a_1 on Cf distribution, it is shown that the rise of β* increases the shear stress at r/R = 0.48, 0.62, 0.82 and 0.95 in the boundary layers along the 45 % of the blade. Whereas, in the rest of the blade surface, the calibration induces a decrease in shear stresses.

3.5.3. 3- turbulent kinetic energy

The effects of β* on turbulent kinetic energy in the blade boundary layers are presented in Fig. 17. The figure shows that higher turbulent kinetic energy is generated on the airfoil upper surface where the flow is accelerated due to circulation around it which gives

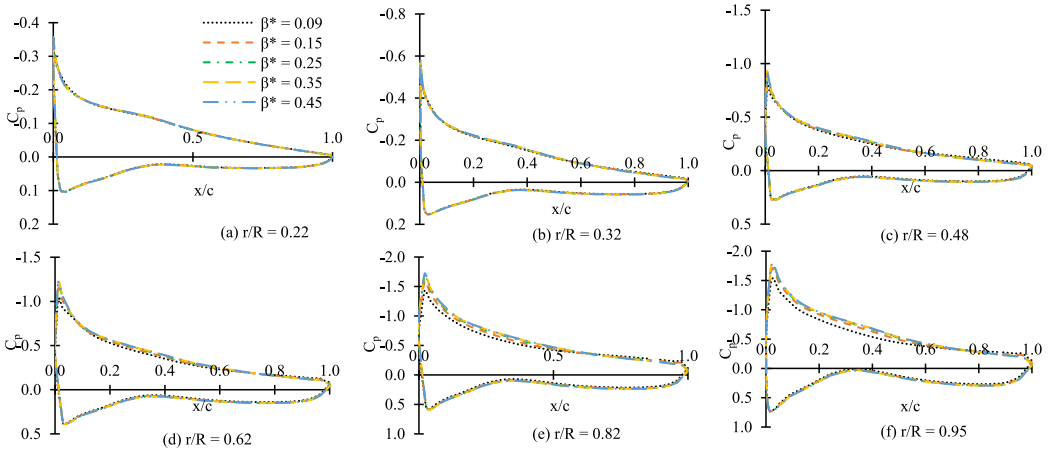

Fig. 12. Pressure coefficient distributions for different values of β* at $a_1 = 0.8$.

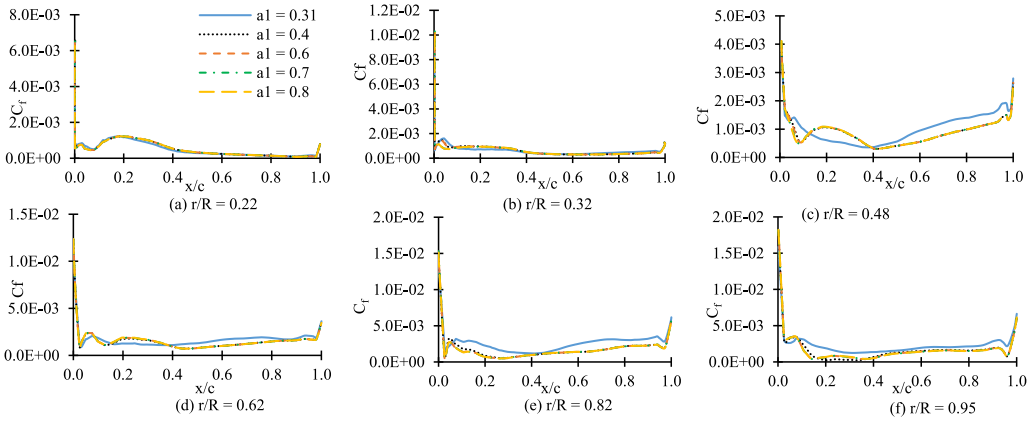

Fig. 13. Skin friction coefficient distributions for different values of a_1 at $\beta^* = 0.09$.

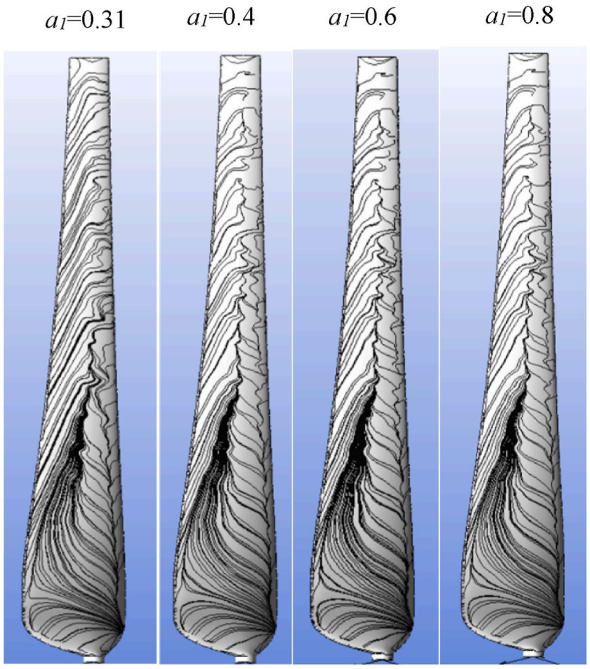

Fig. 14. Streamlines on blade suction side at different values of a_1.

rise to important velocity gradients. Furthermore, a sharp increase of turbulent kinetic energy is recognised near trailing edge, where strong reverse flow exists as a result of flow separation [26].

By the application of the calibration, the increase of β*, decreases the turbulent kinetic energy generated near the leading edge till it achieves minimum values especially near hub region, which leads to an earlier reattachment. Similarly, the increase of β* reduces the turbulent kinetic energy near trailing edge owing hence to vortex strength limitation at this region, which decreases lift losses and enhances rotor efficiency.

4. Conclusion

The flow around a rotor operating near stall condition is highly complex. A good prediction of wind turbine aerodynamics at this condition depends mainly on turbulence model. In order to enhance the potential of the k–ω SST turbulence model in predicting wind turbine efficiency near stall condition, a calibration method of turbulence model coefficients has been proposed. The precited method was applied to NREL S826 NTNU. Ansys Fluent software was used to execute the numerical simulations. On the basis of the results analysis, the main important findings are presented below.

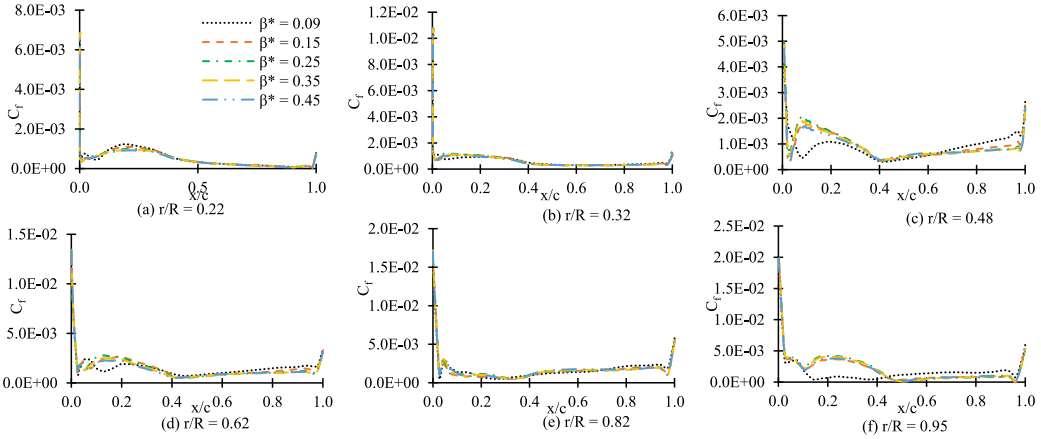

Fig. 15. Skin friction coefficient distributions for different values of β^* at $a_1 = 0.8$.

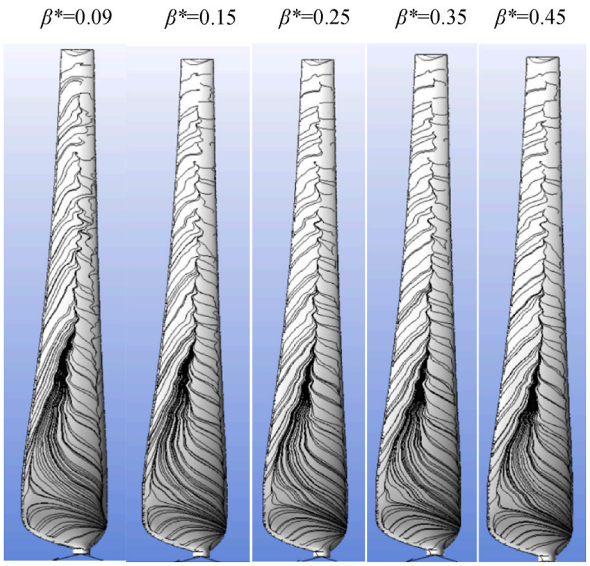

Fig. 16. Streamlines on blade suction side at different values of β* when $a_1 = 0.8$.

- The numerical simulation using k–ω SST turbulence model under-predicts the aerodynamic power coefficient in light stall condition. Whilst, the model shows good results in fully stall condition and in the case where the flow is totally attached.
- Calibration method consists in finding the optimal values of a_1 and β* coefficients responsible for separation control and turbulent kinetic energy dissipation respectively. The relative error of the numerical predicted power coefficient in light stall zone which was under-predicted about 17.89 %, is reduced to 4.58 % by calibration application.
- Calibration method has important effects on blade suction side flow behaviour prediction. The increase of a_1 helps to reduce recirculation zone by delaying separation, while the rising of β* shifts the reattachment upstream, and limits the strength of vortex shedding near trailing edge region.

By applying calibration method, an enhancement of the potential of the k–ω SST turbulence model in predicting wind turbine aerodynamic near light stall condition, is achieved. However, the findings of this study need to be more tested and validated to conclude about calibration method. Further model correction is recommended to develop more accurate model.

Funding

This research received no external funding.

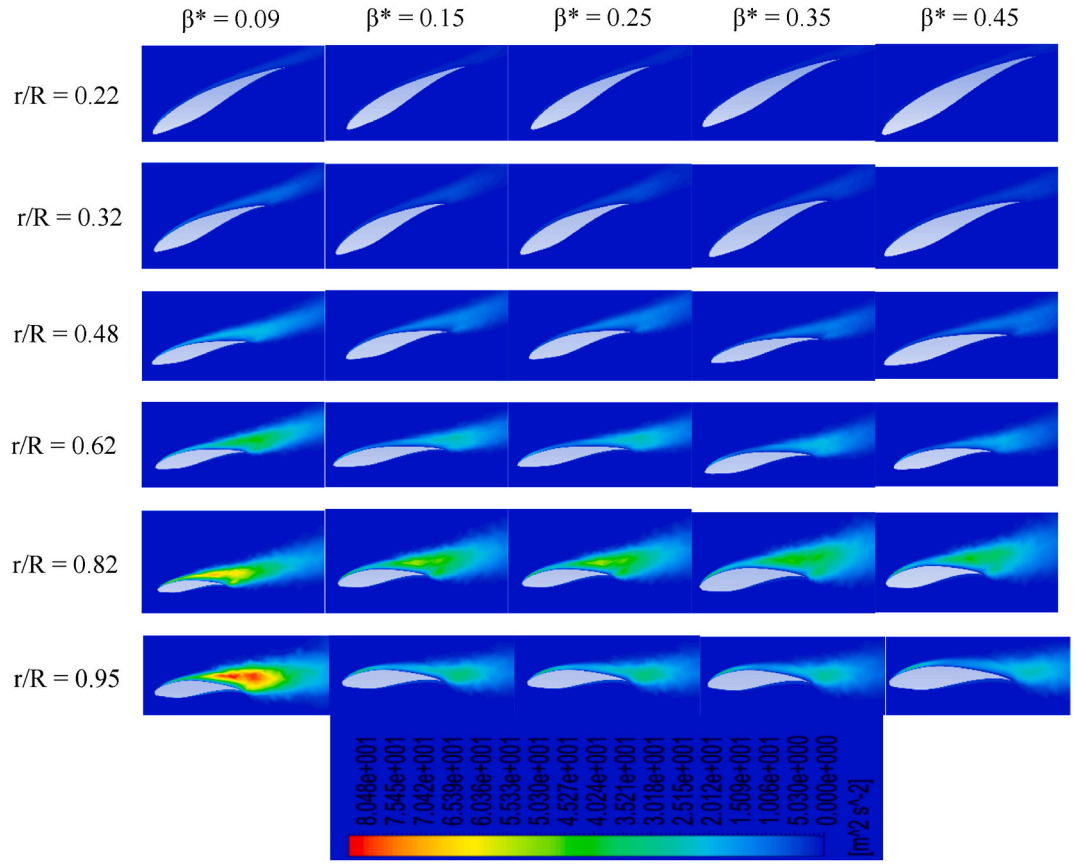

Fig. 17. Turbulence kinetic energy contours around blade for different value of β* at $a_1 = 0.8$.

Data availability statement

Not applicable.

CRediT authorship contribution statement

Somaya Younoussi: Conceptualization, Formal analysis, Investigation, Methodology, Resources, Software, Visualization, Writing - original draft, Writing - review & editing. **Abdeslem Ettaouil:** Project administration, Supervision, Validation.

Declaration of competing interest

The authors declare that they have no known competing financial interests or personal relationships that could have appeared to influence the work reported in this paper.

References

[1] Alex, Global Wind Report 2022, Global Wind Energy Council, 2022. https://gwec.net/global-wind-report-2022/.
[2] Iranzo, CFD applications in energy engineering research and simulation: an introduction to published, Reviews, Processes 7 (2019) 883, https://doi.org/10.3390/pr7120883.
[3] P. Spalart, Detached-eddy simulation, Annu. Rev. Fluid Mech. 41 (2009) 181–202, https://doi.org/10.1146/annurev.fluid.010908.165130.
[4] Y. Zhiyin, Large-eddy simulation: past, present and the future, Chin. J. Aeronaut. 28 (2015) 11–24, https://doi.org/10.1016/j.cja.2014.12.007.
[5] N.A. Che Sidik, S.N.A. Yusof, Y. Asako, S. Mohamed, A. Aziz, A short review on RANS turbulence models, CFD Lett. 12 (2020) 83–96, https://doi.org/10.37934/cfdl.12.11.8396.
[6] H. Rahimi, B. Dose, I. Herraez, J. Peinke, B. Stoevesandt, DDES and URANS comparison of the NREL phase-VI wind turbine at deep stall, in: 34th AIAA Applied Aerodynamics Conference, American Institute of Aeronautics and Astronautics, n.d. https://doi.org/10.2514/6.2016-3127.
[7] Y. Zhang, S. Deng, X. Wang, RANS and DDES simulations of a horizontal-axis wind turbine under stalled flow condition using OpenFOAM, Energy 167 (2019) 1155–1163, https://doi.org/10.1016/j.energy.2018.11.014.
[8] S. Purohit, I.F.S.A. Kabir, E.Y.K. Ng, On the accuracy of uRANS and LES-based CFD modeling approaches for rotor and wake aerodynamics of the (new) Mexico wind turbine rotor phase-III, Energies 14 (2021) 5198, https://doi.org/10.3390/en14165198.

[9] P.A.C. Rocha, H.H.B. Rocha, F.O.M. Carneiro, M.E. Vieira da Silva, A.V. Bueno, k–ω SST (shear stress transport) turbulence model calibration: a case study on a small scale horizontal axis wind turbine, Energy 65 (2014) 412–418, https://doi.org/10.1016/j.energy.2013.11.050.
[10] P.A.C. Rocha, H.H.B. Rocha, F.O.M. Carneiro, M.E.V. da Silva, C.F. de Andrade, A case study on the calibration of the k–ω SST (shear stress transport) turbulence model for small scale wind turbines designed with cambered and symmetrical airfoils, Energy 97 (2016) 144–150, https://doi.org/10.1016/j.energy.2015.12.081.
[11] A.A. Matyushenko, A.V. Garbaruk, Adjustment of the k-ω SST turbulence model for prediction of airfoil characteristics near stall, J. Phys.: Conf. Ser. 769 (2016) 012082, https://doi.org/10.1088/1742-6596/769/1/012082.
[12] W. Zhong, H. Tang, T. Wang, C. Zhu, Accurate RANS simulation of wind turbine stall by turbulence coefficient calibration, Appl. Sci. 8 (2018) 1444, https://doi.org/10.3390/app8091444.
[13] F.R. Menter, Two-equation eddy-viscosity turbulence models for engineering applications, AIAA J. 32 (1994) 1598–1605, https://doi.org/10.2514/3.12149.
[14] B.E. Launder, D.B. Spalding, The numerical computation of turbulent flows, Comput. Methods Appl. Mech. Eng. 3 (1974) 269–289, https://doi.org/10.1016/0045-7825(74)90029-2.
[15] D.A. Johnson, L.S. King, A mathematically simple turbulence closure model for attached and separated turbulent boundary layers, AIAA J. 23 (1985) 1684–1692, https://doi.org/10.2514/3.9152.
[16] Per-Age Krogstad, Pal Egil Eriksen, Jens Andreas Melheim, Blindtest" Workshop Calculations for a Model Wind Turbine, 2011.
[17] T. Ahmad, S.L. Plee, J.P. Myers, Fluent Theory Guide, 2013.
[18] P. Spalart, S. Allmaras, A one-equation turbulence model for aerodynamic flows, in: 30th Aerospace Sciences Meeting and Exhibit, American Institute of Aeronautics and Astronautics, Reno,NV,U.S.A., 1992, https://doi.org/10.2514/6.1992-439.
[19] Suhas V. Patankar, Numerical Heat Transfer and Fluid Flow, first ed., CRC Press, 1980 https://doi.org/10.1201/9781482234213.
[20] R. Bai, J. Li, F. Zeng, C. Yan, Mechanism and performance differences between the SSG/LRR-ω and SST turbulence models in separated flows, Aerospace 9 (2021) 20, https://doi.org/10.3390/aerospace9010020.
[21] F.R. Menter, R. Sechner, A. Matyushenko, Best Practice: RANS Turbulence Modeling in Ansys CFD, (n.d.).
[22] R. Bai, J. Li, F. Zeng, C. Yan, Mechanism and performance differences between the SSG/LRR-ω and SST turbulence models in separated flows, Aerospace 9 (2021) 20, https://doi.org/10.3390/aerospace9010020.
[23] R. Bai, J. Li, F. Zeng, C. Yan, Mechanism and performance differences between the SSG/LRR-ω and SST turbulence models in separated flows, Aerospace 9 (2021) 20, https://doi.org/10.3390/aerospace9010020.
[24] M. Bhotvawala, The k-Omega SST model in OpenFOAM (n.d.), https://mustafabhotvawala.com/wp-content/uploads/2020/11/kOmegaSST.pdf.
[25] L. Shi, Y. Wang, A.-C. Bayeul-Laine, O. Coutier-Delgosha, Numerical investigations on transitional flows around forward and reversed hydrofoils, Eur. J. Mech. B Fluid 85 (2021) 24–45, https://doi.org/10.1016/j.euromechflu.2020.08.008.
[26] G. Jones, M. Santer, G. Papadakis, Control of low Reynolds number flow around an airfoil using periodic surface morphing: a numerical study, J. Fluid Struct. 76 (2018) 95–115, https://doi.org/10.1016/j.jfluidstructs.2017.09.009.